Nonlinear Dyn (2024) 112:2501–2521
https://doi.org/10.1007/s11071-023-09164-5

ORIGINAL PAPER

Dynamic modeling and vibration analysis of double row cylindrical roller bearings with irregular-shaped defects

Xinbin Li · Jing Liu · Shizhao Ding · Yajun Xu · Yu Zhang · Min Xia

Received: 19 May 2023 / Accepted: 13 November 2023 / Published online: 29 December 2023

Abstract Defects in the bearings greatly affect vibrations and performances of rotating transmission systems. Moreover, most previous works estimated the defect shape as a regular shape. However, the actual defect shape is not actually regular. To obtain more accurate vibration characteristics of a defective double row cylindrical roller bearing, an irregular-shaped defect modeling method and a dynamic model of double row cylindrical roller bearing with irregular-shaped defects are proposed in this paper. The dynamic model includes all components and their interactions. A test verification is proposed to validate the established model. The effects of the bearing load, rotating speed, and different independent shape defect sizes on the double row cylindrical roller bearing vibrations are investigated. The comparisons of vibrations between the irregular defect shape and simplified defect shape are studied. The results show that the simplified defect shape model will cause the vibrations to be overestimated. The established dynamic model with the actual defect is more reasonable than the simplified defect model. Moreover, this paper can provide a comprehensive analytical method for double row cylindrical roller bearing vibrations.

Keywords Double row cylindrical roller bearing · Independent defect model · Dynamic modeling · Vibration analysis

X. Li · J. Liu (✉) · Y. Xu
School of Marine Science and Technology, Northwestern Polytechnical University, Xi'an 710072, People's Republic of China
e-mail: jliu@cqu.edu.cn

X. Li · J. Liu · Y. Xu
Laboratory for Unmanned Underwater Vehicle, Northwestern Polytechnical University, Xi'an 710072, People's Republic of China

S. Ding
College of Mechanical Engineering, Chongqing University, Chongqing 400030, People's Republic of China

Y. Zhang
Department of Aeronautical and Automotive Engineering, Loughborough University, Loughborough LE11 3TU, UK

M. Xia
Department of Engineering, Lancaster University, Lancaster LA1 4YW, UK

List of symbols

C_s	The contact damping ratio
C_h	The damping ratio of radial
$f_{1x/y}^{in}$ and $f_{2x/y}^{in}$	The friction forces of first and second rows between the inner ring and roller
$f_{1x/y}^{out}$ and $f_{2x/y}^{out}$	The friction forces of first and second rows between the inner ring and roller
f_{cx} and f_{cy}	The friction forces between the cage and roller

${F_{1x/y}}^{in}$ and ${F_{2x/y}}^{in}$	The total contact forces between roller and inner ring of first and second rows in the *X*/*Y* direction
${F_{dx1}}^{in}$ and ${F_{dx2}}^{in}$	The damping forces of first and second rows between the inner ring and roller in the *X* direction
${F_{dy1}}^{in}$ and ${F_{dy2}}^{in}$	The damping forces of first and second rows between the inner ring and roller in the *Y* direction
${F_x}^{out}$ and ${F_y}^{out}$	The forces of bearing
${F_{1x/y}}^{out}$ and ${F_{2x/y}}^{out}$	The total contact forces between the first and second rows of roller and inner ring
${F_{dx/y1}}^{out}$ and ${F_{dx/y2}}^{out}$	The damping forces of the first and second rows between the outer ring and roller
F_{cx} and F_{cy}	The components of impact between the cage and roller
F_{cj} and f_{cj}	The roller-cage impact and friction forces
k	Time-varying contact stiffness
k_m	The friction coefficient
k_h	The radial contact stiffness
k_s	The contact stiffness of radial
k_c	The roller-cage contact stiffness
L	The width of defect
L_s and h_s	The defect length and depth
L_1	The cage guide surface width
m_{in}	The inner ring mass
m_{out}	The outer ring mass
m_c and I_c	The cage mass and rotational inertia
m_r and φ_r	The roller mass and the angular displacement of roller around the roller center
${P_j}^{out}$	The contact coefficient between the roller and outer ring
x_{in} and y_{in}	The inner ring displacement
${x_j}^r$ and ${y_j}^r$	The *j*-th roller displacements
x_{out} and y_{out}	The outer rings displacements
${x_j}^r$ and ${y_j}^r$	The *j*-th roller displacements
v_L and v_h	The ratios of the defect length and depth
Z	The roller number of one row of DCRB
δ_c	The roller-cage contact deformation
θ_{cage}	The cage angular displacement
θ_r	The angular displacement of roller around the bearing center
${\delta_j}^{out}$	The deformation between the outer ring and *j*-th roller

Abbreviations

TVCS	Time-varying contact stiffness
ECL	The effective contact length

1 Introduction

Roller bearings are the essential components of rotating transmission systems. A higher failure rate of double row cylindrical roller bearings is caused by rough operation conditions. 30% faults of rotating machinery are caused by the bearings [1]. The defects in the double row cylindrical roller bearings will cause safety problems for the whole system. It is useful to study the dynamics of defective double row cylindrical roller bearings, especially for the defects with the actual shapes rather than the simplified shapes including the rectangles and circles.

Many researchers have conducted different dynamic models and detection methods of local defects in the bearings [2–9]. Liu et al. [10, 11] established dynamic models of bearing with the defect including the time-varying contact stiffness (TVCS), edge shapes of the defect, and rotor deformations on the vibrations. In their works, they modeled the defect with a rectangle shape. Chen and Kurfess [12] established a dynamic model to estimate the effects of rectangle shape defect sizes on bearing vibrations. Gao et al. [13] modeled the defect with a rectangle shape and investigated the bearing dynamics of the bearing including the defect on the rings. Cao et al. [14] established a defect model with a rectangle shape and introduced the defect model to the bearing dynamic model to investigate the effects of deflections and defects on the bearing vibrations. Niu et al. [15] presented a dynamic model of roller bearing including the bearing slipping, size, and defect of roller. They also modeled the roller defect with a rectangle shape. Liu and Wang [16] gave a dynamic model including the defect roughness to analyze the effect of the roughness on the vibrations. The defect was also modeled with the rectangle shape [17]. Arslan and Aktu [18] conducted a dynamic model including the rectangle shape defect of ball to evaluate the effect of the defect on the vibrations. Patil et al. [19] gave a bearing dynamic model including the rectangle shape defect to detect the defect vibrations. Patel and Upadhyay [20] gave a bearing model including the deflection of roller, clearance, and rectangle shape defect of roller. Patra et al. [21] introduced the dynamic model of bearing-rotor system including the rotor unbalance forces to discuss the vibrations. Ali et al. [22] presented a combined model using the mass-lumped and finite element models of roller bearing with the rectangle shape defect. Jiang et al. [23] gave a method to describe the roller movement during the defect area taking into account the ring groove radius. Francesco et al. [24] conducted experiments on bearings with different sloped defect edges. They pointed the defect edge characteristics have a remarkable effect on the bearing vibrations. Wang et al. [25] presented an improved defect modeling model by analyzing the bearing vibration and acoustic signals. It can be found that all the above studies use the rectangle shape to model the bearing defect. Moreover, some scholars used hexagons [26], bias rectangles [27], three-dimensional cubic [23, 28], and circular shapes [26] to establish the bearing defect. However, unfortunately, they still use regular shapes to model the bearing defect.

Through the above analysis, it can be found that most previous works focused on studying the single-row bearing dynamic modeling method. The double row cylindrical roller bearings have a more complex structure, which will cause different dynamic characteristics. Moreover, most previous works simplified the defects to a regular shape to estimate the vibrations of the bearing. In fact, the actual defects are irregularly shaped. The regular shapes cannot accurately describe the shape of the bearing defect. Only by getting rid of the restriction of regular shapes can we accurately describe faults. In this paper, an irregular shape defect modeling method and a dynamic model of a double row cylindrical roller bearing with irregular shape defects are proposed. The dynamic model considers the supporting stiffness of the outer ring and the dynamics of the cage, making it better able to reflect the dynamics of the bearing. Moreover, the proposed dynamic model can be used to study the special dynamics of double row cylindrical roller bearings. In addition, for obtaining accurate calculation results of a defective double row cylindrical roller bearing, the defect shape should be the actual shape rather than the simplified shape, which was not considered in the previous studies. The effects of the bearing load, rotating speed, and different independent defect shapes on the vibrations are studied. The comparisons of vibrations between the independent defect shape and simplified defect shape are discussed.

2 An irregular defect shape model for double row cylindrical roller bearings

The dynamics of double row cylindrical roller bearings have strong nonlinearities. Firstly, the contact between the roller and the ring is Hertzian contact theory, and the relationship between the contact force and contact deformation is not linear. Secondly, the revolution of the bearing roller causes changes in the loaded area, which intensifies the non-linearity of the bearing. In addition, the bearing clearance is also one of the sources of bearing nonlinearity. Finally, when the bearing has a defect, especially in the case of an irregular shape defect, the contact deformation and contact stiffness between the roller and ring in the defect area are both nonlinear, which exacerbates the nonlinearity of the bearing [29, 30]. In this work, the nonlinearity sources mentioned above are all considered, and a dynamic model of a double row cylindrical roller bearing with an irregular shape defect is proposed.

2.1 Modeling irregular defect shape

Figure 1 gives independent and simplified defect profiles. The defect edge will generate elastic deformation when the roller contacts with the defect [31], which will change the contact characteristics between the roller and the defective ring. However, the effect of defect edge elastic deformation on the bearing vibration is not the study focus of this work. Thus, the elastic deformation of the material at the defect edge is not considered in this work. Because of the decrement of material of the defect zone on the ring surface, the roller ECL between the roller and ring will decrease. It can cause the TVCS features. The modeling method of TVCS caused by the defect is as follows. (1) The effective contact length (ECL) between the roller and ring should decrease. (2) The ring cross-section area and the area moment of inertia are changed [32, 33].

For simulating the time-varying stiffness features caused by the defect, the main issue is the method for simulating the changes in ECL and cross-section

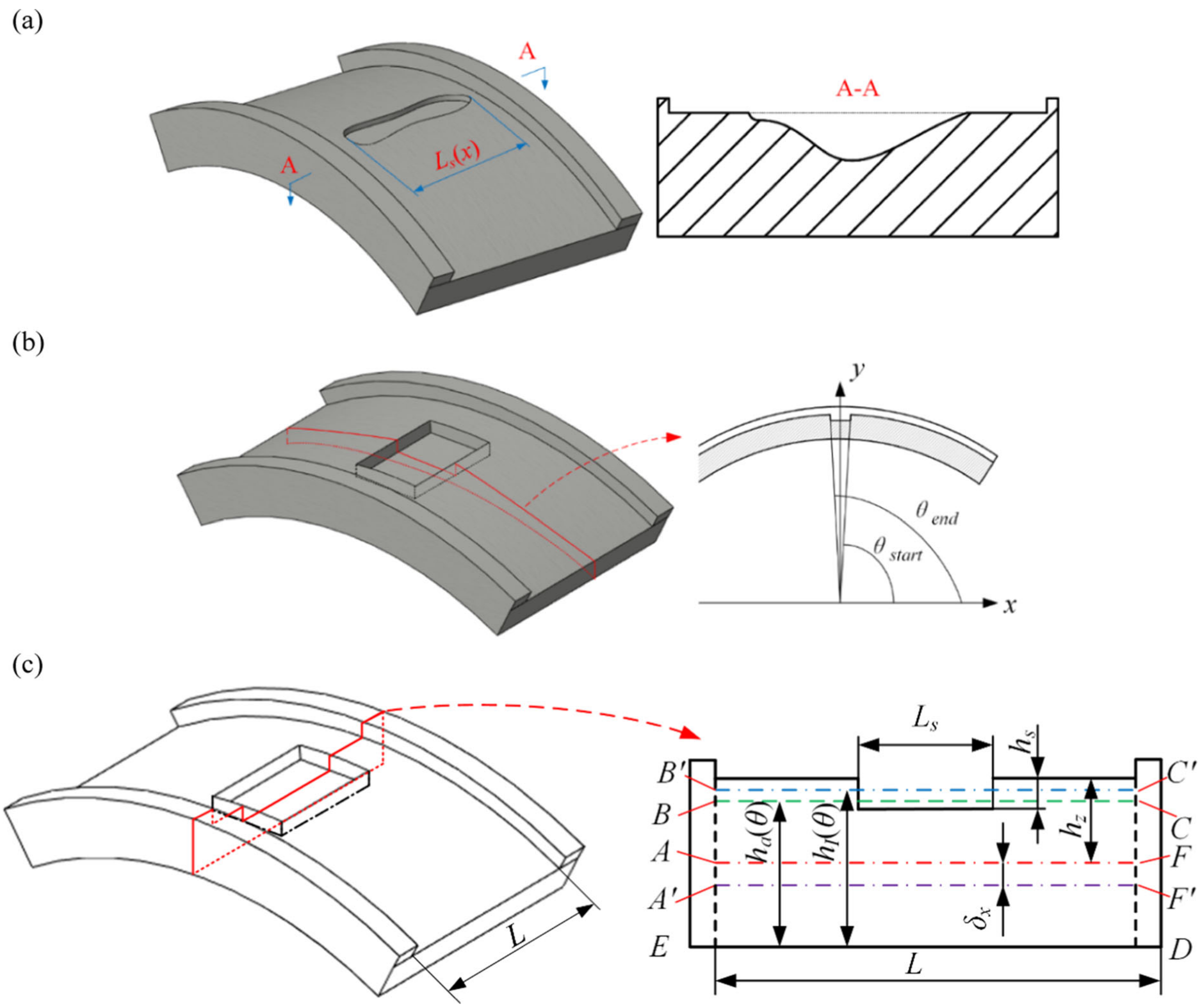

Fig. 1 A diagram of **a** defect profile, **b** circle cross-section profile of rectangular defect, and **c** radial cross-section profile of defect

characteristics. The traditional defect modeling simulated the shape of a defect by simplifying the shape of defect to be a rectangle and a circle. The simplified form was used to simulate the ECL and cross-section characteristics and calculate the TVCS features between the roller and ring. In fact, the simplified shape methods are not accurate as discussed in the above descriptions.

In the model of independent defect shape, the ECL and cross-section characteristics are represented by the function rather than the constant values. Therefore, $L_e = f_L(\theta)$, $A = f_A(\theta)$, and $I = f_I(\theta)$; where L_e is the ECL; A and I are the cross-section area and the moment of inertia; $f_L(\theta)$, $f_A(\theta)$, and $f_I(\theta)$ are the expressions of ECL, cross-section area, and moment of inertia; θ is the angular displacement given in Fig. 1b. The values of $f_L(\theta)$, $f_A(\theta)$, and $f_I(\theta)$ are based on the severity of defect.

Two rectangles BCDE and B'C'DE are given in Fig. 1c, which are used to explain the changes in the defect area. Then, $f_A(\theta)$ and $f_I(\theta)$ are

$$f_A(\theta) = S_{BCDE} = Lh_a(\theta) \tag{1}$$

$$f_I(\theta) = I_{B'C'DE} = \frac{h_I(\theta)^3 L}{12} \tag{2}$$

where S_{BCDE} is the area of rectangle BCDE; $h_a(\theta)$ is the rectangle BCDE height; $I_{\mathrm{B'C'DE}}$ and $h_I(\theta)$ are the rectangle B'C'DE moment of inertia and height; and L is the width of the roller.

For the simple rectangular defects, the cross-section area at θ is

$$A_\theta = 2L_s h_z - L_s h_s \quad \theta \in [\theta_{start}, \theta_{end}] \tag{3}$$

where L_s and h_s are the defect length and depth. The change (δ_x) of neutral axis of inertia moment is

$$\delta_x = \frac{(h_z - 1/2h_S)L_S h_S}{A_\theta} \tag{4}$$

Then, the inertia moment of neutral axis *A'F'* for the defect condition is

$$I_\theta = \frac{2Lh_z^3}{3} + 2Lh_z\delta_x - (\frac{L_s h_s^3}{12} + L_s h_s (h_z - 0.5h_z + \delta_x)^2) \quad \theta \in [\theta_{start}, \theta_{end}] \tag{5}$$

Therefore, the corresponding thickness of rectangle $h_a(\theta)$ and corresponding inertia moment of rectangle $h_I(\theta)$ are

$$h_a(\theta) = \frac{A_\theta}{L} \tag{6}$$

$$h_I(\theta) = (\frac{12I_\theta}{L})^{\frac{1}{3}} \tag{7}$$

Equations (1) and (2) can be also written as

$$f_A(\theta) = 2L_s h_z - L_s h_s \quad \theta \in [\theta_{start}, \theta_{end}] \tag{8}$$

$$f_I(\theta) = \frac{2Lh_z^3}{3} + 2Lh_z\delta_x - (\frac{L_s h_s^3}{12} + L_s h_s (h_z - 0.5h_z + \delta_x)^2)\theta \in [\theta_{start}, \theta_{end}] \tag{9}$$

The defect coefficients are

$$v_L = \frac{L_s}{L} \tag{10}$$

$$v_h = \frac{h_s}{2h_z} \tag{11}$$

where v_L and v_h are the ratios of the defect length and depth at θ. Based on Eqs. (3) to (9), the effective section area is

$$A_\theta = 2Lh_z(1 - v_L v_h) \tag{12}$$

Based on Eqs. (6) to (7), the equivalent inner ring thickness $h_a(\theta)$ is

$$h_a(\theta) = 2(1 - v_L v_h)h_z \tag{13}$$

Based on Eqs. (5) to (9), the inertia moment of the rectangle $h_I(\theta)$ is

$$h_I(\theta) = 2h_z(K_I)^{\frac{1}{3}} \tag{14}$$

$$K_I = \frac{1 - v_h^5 v_L^3 + (4v_h^2 - 6v_h^3 - 5v_h^4)v_L^2 - (5v_h + 4v_h^3 + -6v_h^2)v_L}{(1 - v_L v_L)^2} \tag{15}$$

Therefore, the relation between $h_a(\theta)$ and $h_I(\theta)$ is

$$h_a(\theta) = K_r h_c(\theta) \tag{16}$$

$$K_r = \frac{K_I^{\frac{1}{3}}}{1 - v_L v_L} \tag{17}$$

Based on the defect coefficient v_L and v_h, the ECL, cross-section area, and moment of inertia are

$$L_e(\theta) = L(1 - v_L) \tag{18}$$

$$A_\theta = Lh_c(\theta) = 2L(1 - v_L v_L)h_x \tag{19}$$

$$I_\theta = \frac{h_I(\theta)^3 L}{12} = \frac{(h_I(\theta))^3 K_I L}{12} \tag{20}$$

Equations (16) to (18) can be used for the healthy and defective conditions. When the ring is healthy, $v_L = 0$ and $K_I = 1$; When the shape of defect is complex, v_L is a function of θ; and v_h is the function of defect depth.

2.2 Calculating TVCS of defect with an irregular shape

The contact relationship of the double row cylindrical roller bearing is given in Fig. 2. When the ring has a defect, the roller-ring contact line will be discontinuous. The actual ECL is less than the roller length. The change of ECL will cause the TVCS changes, which affect the vibrations of the double row cylindrical roller bearing.

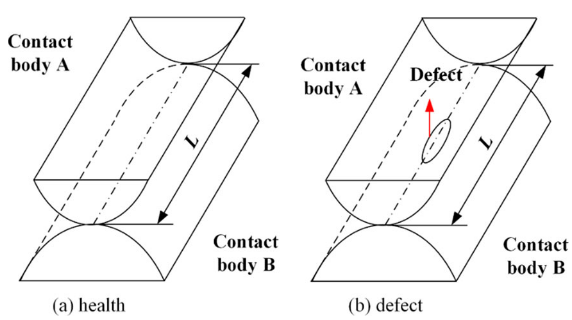

Fig. 2 A diagram of the roller-ring contact relationship

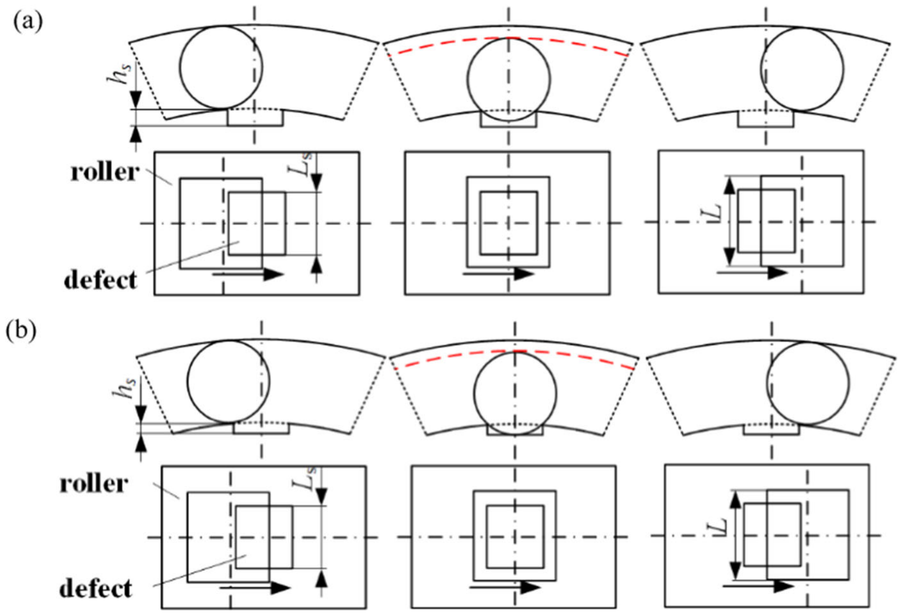

Fig. 3 **a** Roller-ring deformation is less than the defect depth and **b** roller-ring deformation is bigger than or equal to defect depth

In previous studies, most researchers defined the defect shapes as regular, square, or circular ones. In actual situations, the shape of defect is complex and irregular. To solve this question, the TVCS calculation method of the defect with the independent shape of a double row cylindrical roller bearing is proposed.

Compared with different stiffness calculation methods, the Palmgren's stiffness calculation method is simple and accurate [34–36], which is

$$k = 8.06 \times 10^4 L_e^{\frac{8}{9}} \tag{21}$$

where L_{e} is the roller effective contact length.

During the processing of roller through the defect area, there are two cases: (1) the roller-ring deformation is less than the defect depth. (2) The roller-ring deformation is bigger than or equal to the defect depth. There will be a displacement jump for the roller at this moment.

When the roller-ring deformation is less than the defect depth, as shown in Fig. 3a, there are three cases: (1) when the roller is coming into the defect, the ECL changes to be smaller than the roller length (because of the existence of defect); (2) when the roller is located into the defect, because the defect depth is large and the time-varying contact deformation is small, the surface of roller doesn't contact with the defect bottom; thus, the part of roller cannot be supported by the ring; (3) when the roller is coming out the defect, the ECL changes to be equal to the one of health condition.

In case 1, the ECL changes to be equal to the one of health condition. The TVCS is

$$k = 8.06 \times 10^4 L^{\frac{8}{9}} \tag{22}$$

In case 2, the defect depth is large; and the time-varying contact deformation is small, the surface of roller does not touch the bottom of defect. The TVCS is

$$k = 8.06 \times 10^4 (L - L_s)^{\frac{8}{9}} \tag{23}$$

The TVCS of case 3 is the same as that case 2.

In Fig. 3b, the roller-ring deformation is bigger than or equal to the defect depth. For cases 1 and 3, the deformation of roller and defect is less than the defect depth. For case 2, the roller-ring deformation is bigger than the defect depth. The roller will contact with the bottom of defect. Therefore, the ECL is approximately equal to the ECL of health conditions. However, the roller has a displacement at this defect. The deformations of inner/outer ring of jth roller are

$$\begin{cases} \delta_j^{in} = \left[x^{\mathrm{in}} - x_j^{\mathrm{r}}\right]\cos\theta_j + \left[y^{\mathrm{in}} - y_j^{\mathrm{r}}\right]\sin\theta_j - C_{\mathrm{r}} \\ \delta_j^{out} = \left[x_j^{r} - x^{\mathrm{out}} - h_{xs}\right]\cos\theta_j + \left[y_j^{\mathrm{r}} - y^{\mathrm{out}} - h_{xy}\right]\sin\theta_j - C_{\mathrm{r}} \end{cases} \tag{24}$$

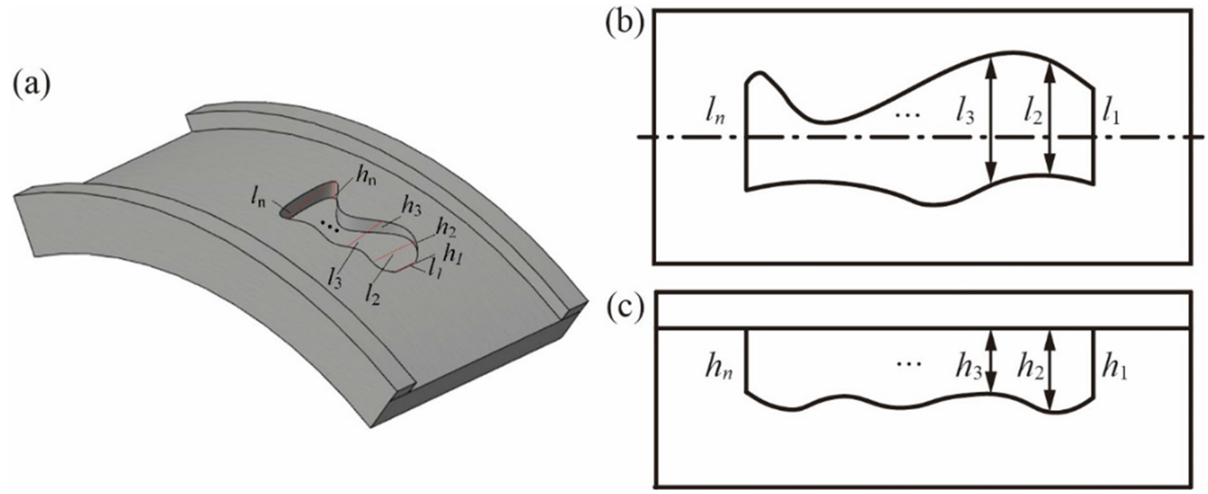

Fig. 4 A diagram for the irregular defect profile

where, x^{in} and y^{in} are the inner ring displacements in x and y directions; x^{out} and y^{out} are the outer ring displacements in x and y directions; x_j^{r} and y_j^{r} are the jth roller displacements in x and y directions; θ_j and C_{r} are the jth roller position angle and bearing clearance; h_{xs} and h_{ys} are the defect depth. Those two situations in this paper can be simulated by the above methods.

The time-varying effective length and depth are used to describe the defect precisely at some moment. The irregular defect is depicted in Fig. 4. Because of the irregular shape of defect, the effective length and the depth are not a constant rather than a function in this paper. The discrete sampling and fitting methods are used to obtain the length and depth of defects. In Fig. 4, l1 to l_{n} is the discrete length of defect at different positions; h_1 to h_{n} is the discrete depth of defect at different positions. Therefore, the functions of length and depth are

$$L_s(\theta)=a_n\theta^n+a_{n-1}\theta^{n-1}+\cdots+a_2\theta^2+a_1\theta+a_0\,\theta\in[\theta_{start},\theta_{end}] \tag{25}$$

$$h_s(\theta)=b_n\theta^n+b_{n-1}\theta^{n-1}+\cdots+b_2\theta^2+b_1\theta+b_0\,\theta\in[\theta_{start},\theta_{end}] \tag{26}$$

where, a_0-a_{n} and b_0-b_{n} are the constant of fitting function, which can be obtained by using the polyfit function in MATLAB. In this work, the defect is divided into six segments for fitting, with 113 sampling points given for each segment, the fitted defect length function is

$$L_s(\theta)=\begin{cases} L-16\times\left(-\sqrt{\dfrac{1.6\times10^{-5}-}{\left(\dfrac{1.6695\times10^{-3}(\theta-\theta_1)}{\theta_2-\theta_1}+1.1589\times10^{-3}\right)^2}}\right. \\ \left.+3.8284\times10^{-3}\right) \quad \theta_1\le\theta<\theta_2 \\ L-1.6\times10^{-2}\ \theta_2\le\theta<\theta_3 \\ L-16\times\left(1\times10^{-3}+\left(\dfrac{\theta-\theta_3}{\theta_4-\theta_3}\times7.071\times10^{-4}\right)^2\right) \quad \theta_3\le\theta<\theta_4 \\ L-16\times\left(\left(\sqrt{1\times10^{-6}-\left(\dfrac{\theta-\theta_4}{\theta_5-\theta_4}\times1.4142\times10^{-3}-7.071\times10^{-4})^2\right.}\right)\right. \\ \left.+1.7071\times10^{-3}-7.071\times10^{-4}\right) \quad \theta_4\le\theta<\theta_5 \\ L-16\times\left(1.7071\times10^{-3}-\left(\dfrac{\theta-\theta_5}{\theta_6-\theta_5}\times7.071\times10^{-4}\right)\right) \quad \theta_5\le\theta<\theta_6 \\ L-\sqrt{1\times10^{-6}-\left(\dfrac{\theta-\theta_4}{\theta_5-\theta_4}\times10^{-3}\right)^2} \quad \theta_6\le\theta<\theta_7 \end{cases}. \tag{27}$$

where θ_1 = 4.6148; θ_2 = 4.6311; θ_3 = 4.6457; θ_4 = 4.7795; θ_5 = 4.7933; θ_6 = 4.8002; θ_7 = 4.8099; moreover, the defect depth in this work is assumed to be constant, which is 20 μm.

3 A dynamic model of the double row cylindrical roller bearing

Figure 5 gives the geometrics of the double row cylindrical roller bearing. The double row cylindrical roller bearing has two rows of rollers that share a common inner ring and outer ring, and two cages. Moreover, each row roller has its own motion state,

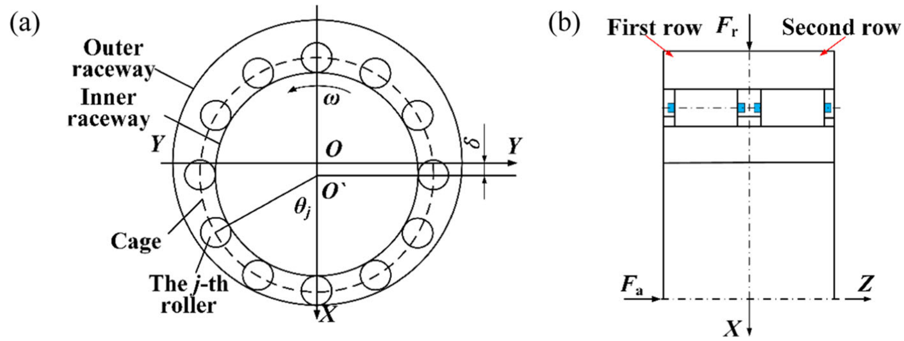

Fig. 5 A diagram of the geometrics of a double row cylindrical roller bearing

and the motions are independent of each other. The bearing rollers contact with the inner ring, outer ring, and the cage beam. The cage will contact with the outer ring. Due to the significant changes in the roller's rotational speed when entering and exiting the load zone, there can be a difference in between the roller rotational speed about the bearing axis and the cage rotational speed, leading to impacts between them. Additionally, due to the roller rotation about its own axis, there will be tangential friction forces generated during the impact moment. The model of double row cylindrical roller bearing established in this work includes roller translation displacements along x and y axes, rotational displacements about z axis and its' own axis, inner/outer ring translation displacements along x and y axes, cage translation displacements along x and y axis, and cage rotational displacements along z axis. The dynamic model is comprehensive and can consider the interaction forces between all components.

3.1 Inner ring kinetic equations

The kinetic equations of inner ring are

$$\begin{cases} m_{\text{in}}\ddot{x}_{\text{in}} = -k_s x_{\text{in}} - F_{1x}^{\text{in}} - F_{2x}^{\text{in}} + f_{1x}^{\text{in}} + f_{2x}^{\text{in}} - F_{dx1}^{\text{in}} - F_{dx2}^{\text{in}} \\ m_{\text{in}}\ddot{y}_{\text{in}} = -k_s y_{\text{in}} - F_{1y}^{\text{in}} - F_{2y}^{\text{in}} + f_{1y}^{\text{in}} + f_{2y}^{\text{in}} - F_{dy1}^{\text{in}} - F_{dy2}^{\text{in}} \end{cases} \tag{28}$$

where, m_{in} is the inner ring mass; x_{in} and y_{in} and are the inner ring displacement; k_{s} is the contact stiffness of radial; $F_{1x/y}{}^{\text{in}}$ and $F_{2x/y}{}^{\text{in}}$ are the total contact forces between roller and inner ring of first and second rows in the X/Y direction; $f_{1x/y}{}^{\text{in}}$ and $f_{2x/y}{}^{\text{in}}$ are the total frictional forces between roller and inner ring of first and second rows in the X/Y direction; $F_{\text{d}x1}{}^{\text{in}}$ and $F_{\text{d}x2}{}^{\text{in}}$ are the damping forces of first and second rows between the inner ring and roller in the X direction; moreover, $F_{\text{d}y1}{}^{\text{in}}$ and $F_{\text{d}y2}{}^{\text{in}}$ are the damping forces of first and second rows between the inner ring and roller in the Y direction; Moreover, $F_{ix}{}^{\text{in}}$ and $F_{iy}{}^{\text{in}}$ are [37, 38]

$$\begin{bmatrix} F_{ix}^{\text{in}} \\ F_{iy}^{\text{in}} \end{bmatrix} = \sum_{j=1}^{Z} \left[K_{\text{i}}(\delta_j^{\text{in}})^n P_j^{\text{in}}\right] \begin{bmatrix} \cos\theta_j \\ \sin\theta_j \end{bmatrix} \quad i = 1,2 \tag{29}$$

where θ_j is the jth roller position angle; K_{i} is the TVCS between the roller and inner ring; n = 10/9; the inner ring contact coefficients $P_j{}^{\text{in}}$ is

$$P_j^{\text{in}} = \begin{cases} 0 & \delta_j^{\text{in}} < 0 \\ 1 & \delta_j^{\text{in}} > 0 \end{cases} \tag{30}$$

where the deformation of inner rings of jth roller $\delta_j{}^{\text{in}}$ is

$$\delta_j^{\text{in}} = [x_{\text{in}} - x_j^r]\cos\theta_j + [y_{\text{in}} - y_j^r]\sin\theta_j - C_r \tag{31}$$

where $x_j{}^{\text{r}}$ and $y_j{}^{\text{r}}$ are the jth roller displacements; C_{r} is the bearing radial clearance; and the roller position angle θ_j is

$$\theta_j = \theta_c + \frac{2\pi(j-1)}{Z} \quad j = 1,2,\ldots,Z \tag{32}$$

where θ_c is the cage angular displacements; Z is the roller number of one row of double row cylindrical roller bearing; $f_{1\text{x/y}}{}^{\text{in}}$ and $f_{2\text{x/y}}{}^{\text{in}}$ are the friction forces of first and second rows between the inner ring and roller, which are

$$\begin{bmatrix} f_{ix}^{\text{in}} \\ f_{iy}^{\text{in}} \end{bmatrix} = \sum_{j=1}^{Z} [k_m K_{\text{i}}(\delta_j^{\text{in}})^n P_j^{\text{in}}] \begin{bmatrix} \cos\theta_j \\ \sin\theta_j \end{bmatrix} \quad i = 1,2 \tag{33}$$

where k_{m} is the friction coefficient. moreover, $F_{\text{d}x/y1}{}^{\text{in}}$ and $F_{\text{d}x/y2}{}^{\text{in}}$ are

$$\begin{bmatrix} F_{\text{d}xi}^{\text{in}} \\ F_{\text{d}yi}^{\text{in}} \end{bmatrix} = \sum_{j=1}^{Z} [c_{\text{c}}\dot{\delta}_j^{\text{in}} P_j^{\text{in}}] \begin{bmatrix} \cos\theta_j \\ \sin\theta_j \end{bmatrix} \quad i = 1,2 \tag{34}$$

where c_c is the contact damping ratio.

3.2 Outer ring kinetic equations

The kinetic equations of outer ring are

$$\begin{cases} m_{out}\ddot{x}_{out} = F_{1x}^{out} + F_{2x}^{out} - C_h\dot{x}_{out} - k_h x_{out} + f_{1x}^{out} + f_{2x}^{out} + F_{dx1}^{out} + F_{dx2}^{out} - F_x^{out} \\ m_{out}\ddot{y}_{out} = F_{1y}^{out} + F_{2y}^{out} - C_h\dot{y}_{out} - k_h y_{out} + f_{1y}^{out} + f_{2y}^{out} + F_{dy1}^{out} + F_{dy2}^{out} - F_y^{out} \end{cases} \tag{35}$$

where, m_{out} is the outer ring mass; $F_x{}^{out}$ and $F_y{}^{out}$ are the external forces between the roller and bearing outer ring; x_{out} and y_{out} are the outer rings displacements; C_h is the damping ratio of radial; k_h is the radial contact stiffness; $f_{1x/y}{}^{out}$ and $f_{2x/y}{}^{out}$ are the total frictional forces between the first and second rows of roller and outer ring; $F_{1x/y}{}^{out}$ and $F_{2x/y}{}^{out}$ are the total contact forces between the first and second rows of roller and outer ring, which are

$$\begin{bmatrix} F_{ix}^{out} \\ F_{iy}^{out} \end{bmatrix} = \sum_{j=1}^{Z} \left[K_e (\delta_j^{out})^n P_j^{out} \right] \begin{bmatrix} \cos\theta_j \\ \sin\theta_j \end{bmatrix} \quad i = 1,2 \tag{36}$$

where K_e is the contact stiffness between the roller and the outer ring; the contact coefficient between the roller and outer ring $P_j{}^{out}$ is

$$P_j^{out} = \begin{cases} 0 & \delta_j^{out} < 0 \\ 1 & \delta_j^{out} > 0 \end{cases} \tag{37}$$

where the deformation between the outer ring and j-th roller $\delta_j{}^{out}$ is

$$\delta_j^{out} = [x_j^r - x_j^{out}]\cos\theta_j + [y_j^r - y_j^{out}]\sin\theta_j \tag{38}$$

where $x_j{}^{out}$ and $y_j{}^{out}$ are the outer ring displacements; $x_j{}^r$ and $y_j{}^r$ are the jth roller displacements; $f_{1x/y}{}^{out}$ and $f_{2x/y}{}^{out}$ are the friction forces of the first and second rows between the inner ring and roller, which are

$$\begin{bmatrix} f_{ix}^{out} \\ f_{iy}^{out} \end{bmatrix} = \sum_{j=1}^{Z} \left[k_m K_e (\delta_j^{out})^n P_j^{out} \right] \begin{bmatrix} \cos\theta_j \\ \sin\theta_j \end{bmatrix} \quad i = 1,2 \tag{39}$$

where $F_{dx/y1}{}^{out}$ and $F_{dx/y2}{}^{out}$ are the damping forces of the first and second rows between the outer ring and roller, which are

$$\begin{bmatrix} F_{dxi}^{out} \\ F_{dyi}^{out} \end{bmatrix} = \sum_{j=1}^{Z} \left[c_c \dot{\delta}_j^{out} P_j^{out} \right] \begin{bmatrix} \cos\theta_j \\ \sin\theta_j \end{bmatrix} \quad i = 1,2 \tag{40}$$

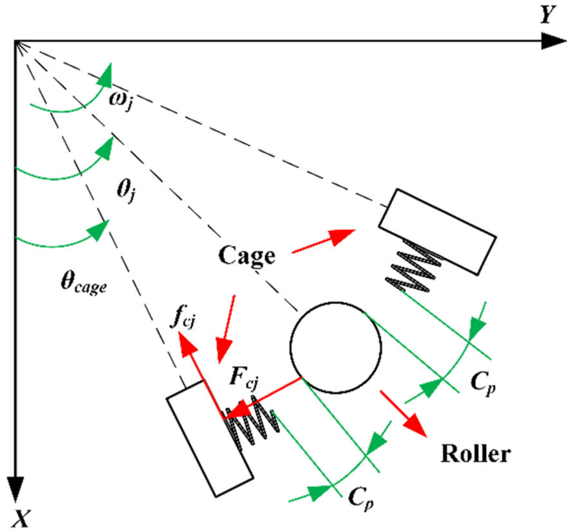

Fig. 6 The relative motion between cage and roller

where c_c is the contact damping ratio.

3.3 Cage kinetic equations

Figure 6 gives the relative motion between the cage and roller. The kinetic equations of outer ring are

$$\begin{cases} m_c\ddot{x}_{ic} = \sum_{j=1}^{Z} (-F_{icx}(j) + f_{icx}(j)) + F_{icx}^{d} & i = 1,2 \\ m_c\ddot{y}_{ic} = \sum_{j=1}^{Z} (-F_{icy}(j) - f_{icy}(j)) + F_{icy}^{d} & i = 1,2 \\ I_c\ddot{\theta}_{ic} = \sum_{j=1}^{Z} (-F_{ic} \times 0.5D_m) + M_c & i = 1,2 \end{cases} \tag{41}$$

where F_{cx} and F_{cy} are the components of impact between the cage and roller; f_{cx} and f_{cy} are the friction forces between the cage and roller; m_c and I_c are the cage mass and rotational inertia; moreover, $F_{icx}{}^{d}$, $F_{icy}{}^{d}$, and M_c are

$$\begin{cases} F_{icx}^{d'} = \dfrac{-\eta_0 u_1 L_1^3 \varepsilon^2}{C_g^2 (1-\varepsilon^2)^2} & i = 1,2 \\ F_{icy}^{d'} = \dfrac{\pi \eta_0 u_1 L_1^3 \varepsilon}{4C_g^2 (1-\varepsilon^2)^{3/2}} & i = 1,2 \\ M_c' = \dfrac{2\pi\eta_0 V_1 R_1^2 L_1}{C_g\sqrt{1-\varepsilon^2}} & i = 1,2 \end{cases} \tag{42}$$

where the lubricating oil traction speed is $u_1 = R_1(-\omega_o + \omega_c)$; L_1 is the cage guide surface width; C_g is the cage guide surface clearance; ε is the cage eccentricity; the relevant parameters are explained in Refs. [39–42].

The resultant forces and moment ${F_{icx}}^d$, ${F_{icy}}^d$, and M_c are

$$\begin{Bmatrix} M_c \\ F_{icx}^d \\ F_{icy}^d \end{Bmatrix} = \begin{bmatrix} 1 & 0 & 0 \\ 0 & \cos\phi_c & -\sin\phi_c \\ 0 & \sin\phi_c & \cos\phi_c \end{bmatrix} \begin{Bmatrix} M_c' \\ F_{icx}^{d'} \\ F_{icy}^{d'} \end{Bmatrix} \tag{43}$$

where, $\varphi_c = \arctan(y_c/x_c)$. F_{cj} and f_{cj} are the roller-cage impact and friction forces. The roller-cage contact is simplified into the spring, and the roller-cage impact force is

$$F_{ic}(j) = k_{ic}(j)\delta_{ic}(j) \quad i = 1,2 \tag{44}$$

where k_c is the roller-cage contact stiffness; the roller-cage contact deformation δ_c is

$$\delta_c(j) = \begin{cases} z_c(j) - C_p & |z_c(j) - C_p| > 0 \\ 0 & |z_c(j) - C_p| = 0 \end{cases} \tag{45}$$

where C_p is the cage pocket clearance; the roller-cage angular displacement difference z_j is

$$z_j(j) = (\theta_{cage} - \theta_j)\frac{D_m}{2} + y_c\cos\theta_j + z_c\sin\theta_j \tag{46}$$

where θ_{cage} is the cage angular displacement.

The roller-cage frictional force is

$$f_c(j) = \mu_c(j)F_c(j) \tag{47}$$

$$\mu_c(j) = (-0.1 + 22.28S(j))e^{-181.46S(j)} + 0.1 \tag{48}$$

where S is the slide-roll ratio of j-th roller. The components of F_c are

$$\begin{cases} F_{icx}(j) = F_{ic}(j)\sin(\theta_j) & i = 1,2 \\ F_{icy}(j) = F_{ic}(j)\cos(\theta_j) & i = 1,2 \end{cases} \tag{49}$$

Therefore, the components of f_c are

$$\begin{cases} f_{icx}(j) = f_{ic}(j)\cos(\theta_j) & i = 1,2 \\ f_{icy}(j) = f_{ic}(j)\sin(\theta_j) & i = 1,2 \end{cases} \tag{50}$$

3.4 Roller kinetic equations

In operation, the roller motion is affected by the bearing cage and rings. The forces applied on the roller

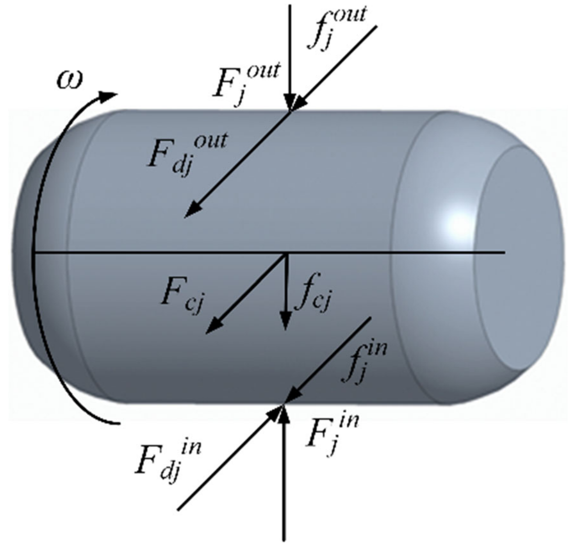

Fig. 7 Forces applied on the roller

are given in Fig. 7. ${F_j}^{in}$ and ${F_j}^{out}$ are the double row cylindrical roller bearing contact forces; ${F_{dj}}^{in}$ and ${F_{dj}}^{out}$ are the oil film resistances between the ring and j-th roller; ${f_j}^{in}$ and ${f_j}^{out}$ are the friction forces between the rings and j-th roller; F_{cj} and f_{cj} are the roller-cage impact and friction forces.

The kinetic equations of roller are

$$\begin{cases} m_r\ddot{x}_j^r = F_{ix}^{in}(j) - F_{ix}^{out}(j) + F_{dxi}^{in}(j) - F_{dxi}^{out}(j) - f_{iy}^{in}(j) + f_{iy}^{out}(j) - F_{icx}(j) + f_{icx}(j) \\ m_r\ddot{y}_j^r = F_{iy}^{in}(j) - F_{iy}^{out}(j) + F_{dyi}^{in}(j) - F_{dyi}^{out}(j) + f_{ix}^{in}(j) - f_{ix}^{out}(j) + F_{icx}(j) + f_{icx}(j) \\ I_r\ddot{\phi}_{ir} = 0.5(f_i^{out}(j) + f_i^{in}(j) - f_{ic}(j))d \\ I_{or}\ddot{\theta}_{ir} = 0.5(D_{out}f_i^{out}(j) - D_{in}f_i^{in}(j) - D_m(F_{ic}(j) + F_{id}(j))) \end{cases} \tag{51}$$

where m_r and φ_r are the roller mass and the angular displacement of roller around the roller center; θ_r is the angular displacement of roller around the bearing center.

4 Results and discussions

4.1 Experimental validation

The dynamic model with the independent defect shape of double row cylindrical roller bearing can be used to calculate the vibrations of inner/outer ring, roller, and cage. A double row cylindrical roller bearing NN3007 of SKF is used to simulate the vibrations. The NN3007 bearing structural parameters are depicted in Table 1.

Table 1 NN3007 bearing structural parameters

Parameter	Value
Inner ring diameter of/D_i	43 mm
Outer ring diameter/D_o	55 mm
Pitch diameter/D_m	49 mm
Roller diameter/d	6 mm
ECL of roller/l	6 mm
Number of roller/Z	19 × 2
Radial clearance/C_r	10 µm
Pocket clearance/C_p	0.09 mm
Guide face-cage clearance /C_g	1 mm
Width of guiding land/L_l	6 mm
Cage outer diameter	53 mm
Cage inner diameter	45 mm
Cage width/C_w	6 mm
Friction coefficient/μ	0.02
Outer ring mass/m_{out}	0.0791 kg
Inner ring mass/m_{in}	0.1010 kg
Roller mass/m_r	0.0013 kg
Cage mass/m_c	0.0148 kg

The stiffness calculation method given by Palmgren can calculate the roller-ring contact stiffness. The contact stiffnesses between the roller and outer/inner ring are 1.898×10^8 N/m^n and 1.828×10^8 N/m^n. The damping ratio between the roller and ring is 200 Ns/m. The initial velocities of roller and ring are 0 m/s. The initial displacements of roller and ring are 10^{-6}m and 10^{-6}m in the X and Y directions.

Figure 8a gives the test instrument named BVT-5. The double row cylindrical roller bearing is mounted on the shaft. The shaft is driven by the electric motor and the rotational speed of the shaft is 1800 r/min. The external force is applied by two loading arms symmetrically distributed along the axis. The radial load is loaded by the force application arm. The acceleration sensor (PCB-352C04) is installed on the bearing outer ring in the X direction. The LMS system and computer are used to acquire the vibration signals of the double row cylindrical roller bearing. The sampling frequency is set to 25,600 Hz. The bearing is NN3007. The radial load is 300 N. To verify the accuracy of model, the rectangle defect (3 mm × 4 mm) in Fig. 8b, the circular defect (diameter 4.5 mm) in Fig. 8c, and the defect with the independent shape in Fig. 8d are studied. The effective roller lengths when the roller rolls over the rectangle defect, the circular defect, and the defect with the independent shape are given in Fig. 9.

4.1.1 *Case study: rectangle defect*

The comparisons of outer ring accelerations in the X direction between the experimental and simulated are given in Fig. 10. In Fig. 10a and b, the defect frequencies of outer ring from the simulated and experimental are 249.60 Hz and 250.97 Hz. Their difference is 0.55%. In Fig. 10c, the simulated results are familiar to the experimental ones. Figure 10d gives the comparisons of the acceleration impacts when the roller enters and exits the defect area between the simulated and experimental results. The simulated results are familiar with the experimental ones, which can validate the proposed model.

4.1.2 *Case study: circular defect*

The comparisons of accelerations of outer ring in the X direction from the experimental and simulated are plotted in Fig. 11. In Fig. 11a and b, the defect frequencies of outer ring of simulated and experimental are 250.39 Hz and 249.23 Hz. Their error is 0.467%. In Fig. 11c, the simulated results are familiar to the experimental ones. Figure 11d gives the comparisons of the acceleration impacts when roller enters and exits the defect area between the simulated and experimental accelerations. The simulated results are familiar with the experimental ones, which can also validate the proposed model.

4.1.3 *Case study: defect with an irregular shape*

The comparisons of accelerations of outer ring in the X direction between the experimental and simulated results are given in Fig. 12. In Fig. 12a and b, the defect frequencies of outer ring of simulated and experimental are 249.40 Hz and 250.21 Hz, respectively. Their error is 0.32%. In Fig. 12c, the simulated results of dynamic model are familiar with the experimental ones. Figure 12d gives the comparisons of the acceleration impacts when roller enters and exits the defect area between the simulated and experimental ones. Similarly, the simulated results are familiar with the experimental results, which can validate the proposed model too.

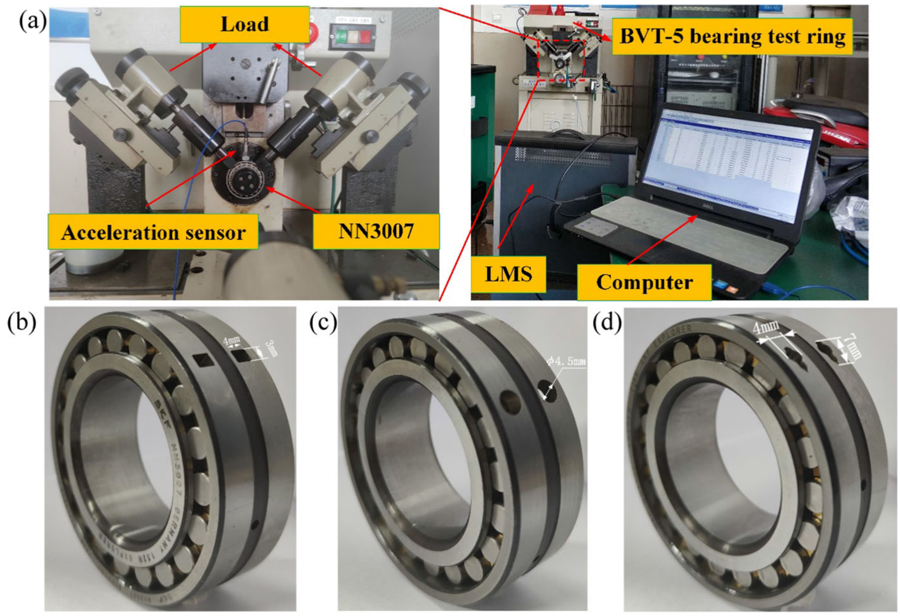

Fig. 8 **a** A bearing vibration test instrument named BVT-5; **b** a rectangle defect case, **c** a circular defect case; and **d** the defect with the independent shape

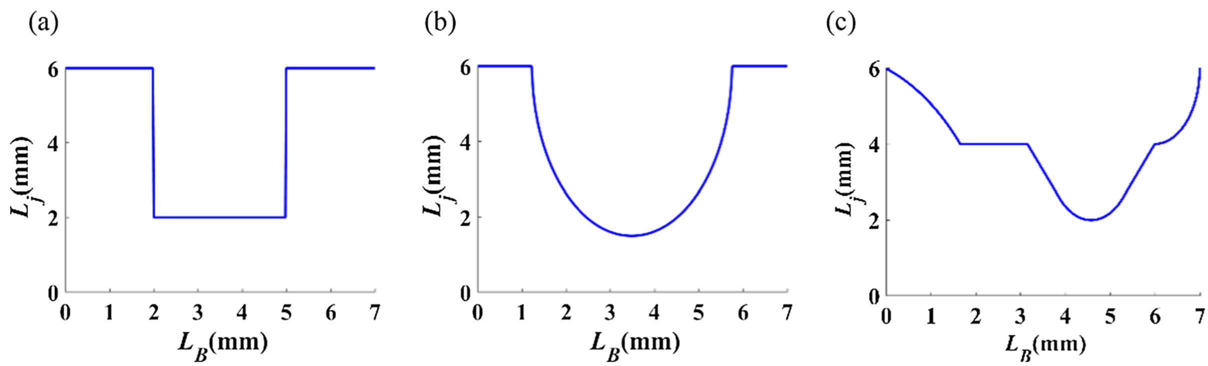

Fig. 9 Time-varying effective roller length for **a** the rectangle defect, **b** the circular defect, and **c** the defect with the independent shape

4.2 Comparative analysis of vibrations between irregular and simplified defect shapes

In the following sections, the initial velocities of roller and ring are their theoretical value under pure rolling conditions. The initial displacements of roller and ring are 10^{-6}m and 10^{-6}m in the X and Y directions. The rotating speed is 1800 r/min. The loads in the X and Y directions are 300 N and 0 N.

In the previous studies, most researchers defined the defect shape as the regular shape including the square or circle, as given in Fig. 13a. This method can simplify the calculation, but the accuracy is low. The independent defect is simplified to be a rectangle (7 mm $\times$ 4 mm) as given in Fig. 13b. The dynamic models with the simplified and independent defect models are simulated, respectively.

In Fig. 14a, the acceleration of the simplified defect is larger than that of the actual defect shape. Figure 14b gives the comparison of TVCS between the simplified defect shape and the actual defect shape. The TVCS of actual defects is more accurate than that of simplified defects. The comparison of defect impact between the simplified defect shape and actual defect shape is given in Fig. 14c. Note that the acceleration peak value of impact of simplified defect is greater than that of the actual defect. There are similarities in the acceleration and impact when the roller enters and

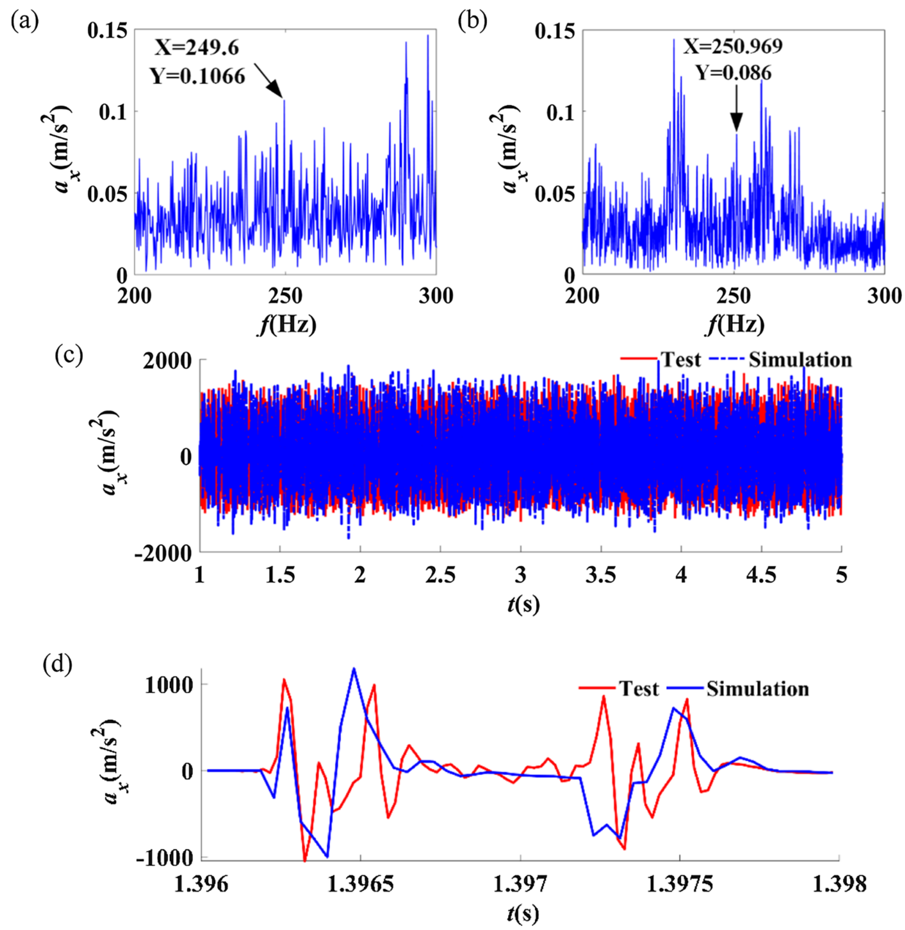

Fig. 10 Comparisons of the experimental and simulated results of outer ring for the rectangular defect case. **a** Simulated spectrum, **b** experimental spectrum, **c** simulated and experimental accelerations, and **d** simulated and experimental accelerations in the defect impact area

exits the defect. When the roller enters the defect, the TVCS and ECL of the simplified defect change greatly, but the TVCS and ECL of the actual defect change slowly, which makes different impact characteristics. Thus, the model with the actual defect is more reasonable than that with the simplified defect.

4.3 Effect of irregular defect sizes on double row cylindrical roller bearing vibrations

To study the effects of independent defect sizes on the bearing vibrations, the maximum width sizes of independent defect are 3 mm, 4 mm, and 5 mm, as shown in Fig. 15. Different maximum width cases cause different areas and ECLs of the defect. Figure 16 gives the outer ring accelerations for the irregular defects with different maximum widths. Note that the outer ring accelerations increase with the increment of the maximum width of the defect. Figure 17 gives the effect of the independent defect with different maximum widths on the accelerations of the inner/ring. Note that the inner/outer ring acceleration RMS values increase with the increment of the maximum width of the defect. Moreover, the accelerations in the *X* direction are larger than those in the *Y* direction.

4.4 Effects of the load and rotating speed on the double row cylindrical roller bearing vibrations for irregular-shaped defect

To study the effects of the rotating speed on the DRCB vibrations, the rotating speeds are 1000 r/min, 2000 r/min, 3000 r/min, 4000 r/min, and 5000 r/min. The

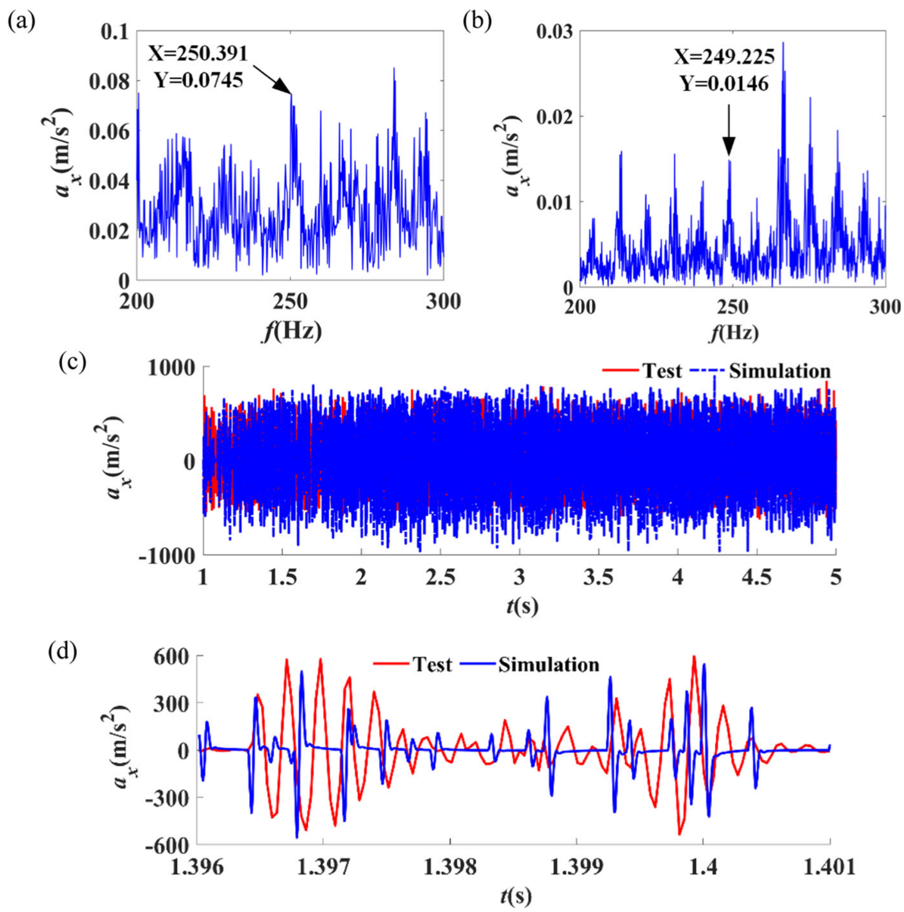

Fig. 11 Comparison of the experimental and simulated results of outer ring for the circular defect case. **a** Simulated spectrum, **b** experimental spectrum, c simulated and experimental accelerations, and **d** simulated and experimental accelerations in the defect impact area

model with the independent defect is used to simulate the accelerations of DRCB. The maximum width of the independent defect is 4mm. Figure 18 gives the effects of the rotating speed on the accelerations of the inner/outer ring and cage. Note that the rotating speed can greatly affect the inner/outer ring and cage vibrations. The inner/outer ring accelerations increase first and then decrease with the increment of the rotating speed. The cage accelerations increase with the increment of the rotating speed.

To illustrate the effect of the load value on the DRCB vibrations, the load is 500 N, 1000 N, 1500 N, 2000 N, and 2500 N. The model with the independent defect is used to simulate the accelerations of DRCB. The maximum width of independent defect is 4 mm. Figure 19 demonstrates the effect of the load on the inner/outer ring and cage accelerations. Note that the load has a remarkable effect on the inner/outer ring and the cage vibrations. The outer ring acceleration in the *Y* direction increases with the increment of the load value. The outer ring accelerations in the *X* direction increase first and then decrease with the increment of the load value. The inner ring accelerations increase with the increment of the load value. The cage accelerations increase first and then decrease with the increment of the load value.

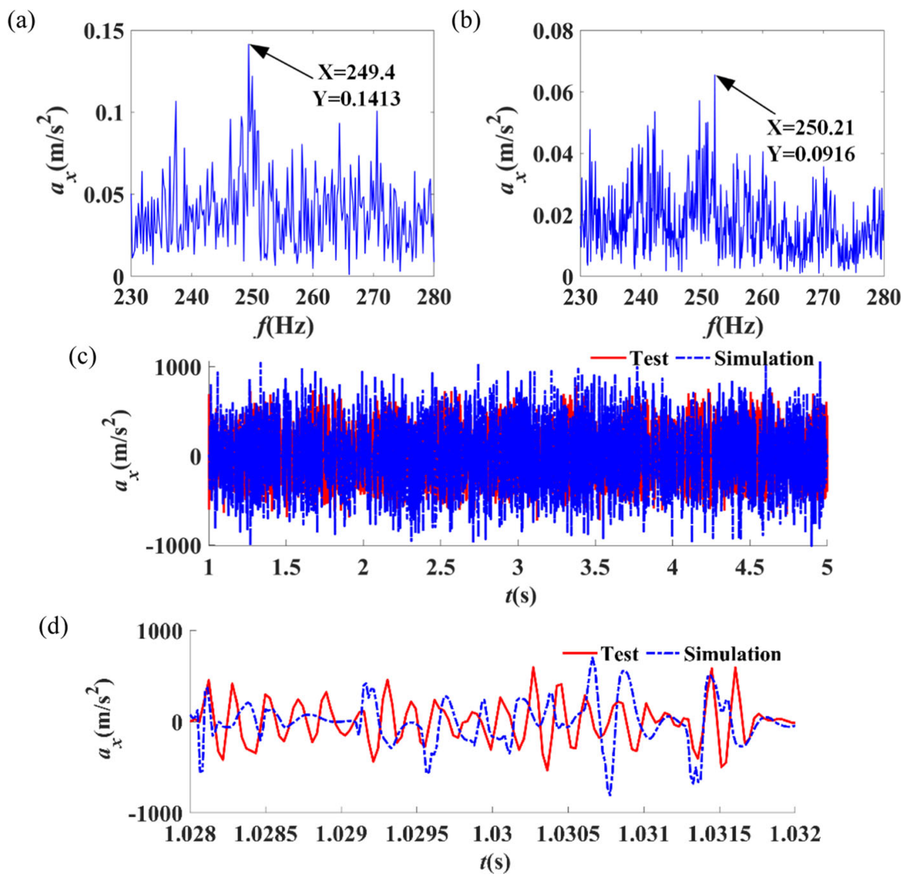

Fig. 12 Experimental and simulated results of outer ring. **a** Frequency-domain simulated signal, **b** frequency-domain experimental signal, **c** simulated and experimental accelerations, and **d** simulated and experimental accelerations in the defect impact area

4.5 Model comparison

To further demonstrate the advancement of the dynamic model and the defect modeling method proposed in this work, the results obtained by the proposed method and the method in Ref. [43] are compared. The defect width is 4 mm. Figure 20a shows the dynamics obtained by the proposed dynamic model coupled with the proposed defect model and the dynamic model in Ref. [43] coupled with the defect model in Ref. [43]. The RMS value of the results obtained by the proposed dynamic model coupled with the proposed defect model is 30.414 m/s^2; while the one of the results obtained by the dynamic model in Ref. [43] coupled with the defect model in Ref. [43] is 29.01 m/s^2. Figure 20b compares the result obtained by the proposed dynamic model coupled with the proposed defect model and the proposed dynamic model coupled with the defect model in Ref. [43]. The RMS value of the results obtained by the proposed dynamic model coupled with the defect model in Ref. [43] is 32.06 m/s^2. Compare the results obtained by the proposed dynamic model coupled with the proposed defect model and the proposed dynamic model coupled with the defect model in Ref. [43], it can be found that the defect modeling method in Ref. [43] will cause the simulation results that are higher than the actual results. Moreover, compare the results obtained by the proposed dynamic model coupled with the proposed defect model and the dynamic model in Ref. [43] coupled with the defect model in Ref. [43], it can be

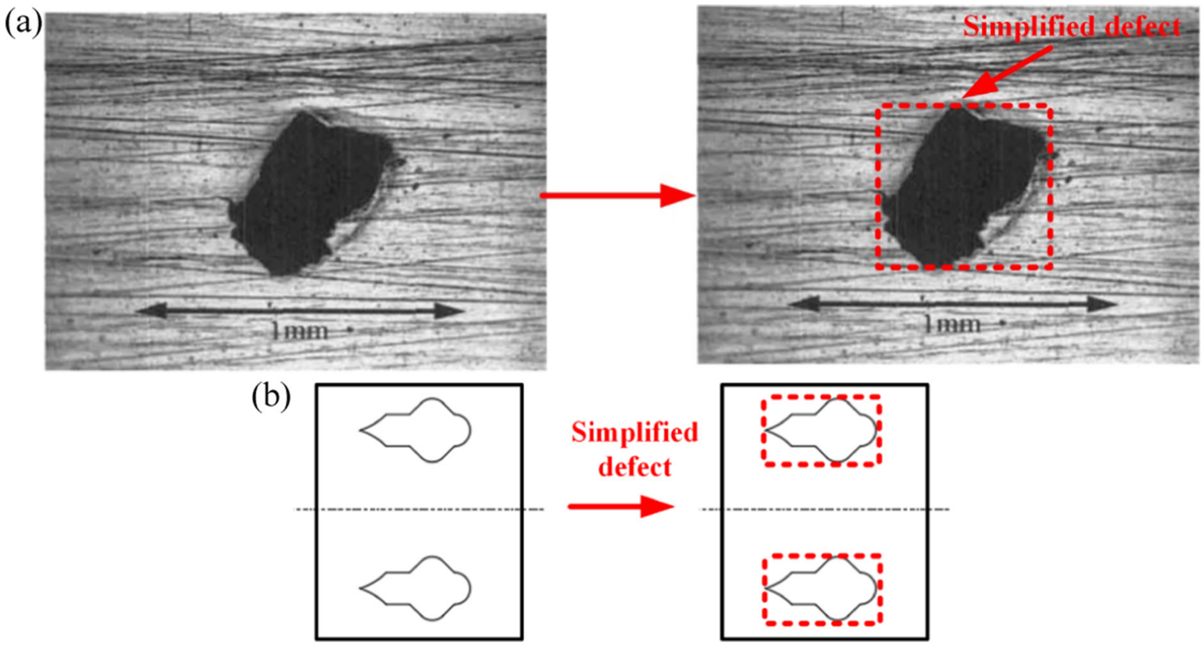

Fig. 13 **a** Traditional defect shape simplification method and **b** simplification of independent defect shape

found that the result obtained by the proposed dynamic model is larger than the one obtained by the dynamic model in Ref. [43], which indicates that the necessity of considering the supporting stiffness of the outer ring and the dynamics of the bearing cage. These can provide some evidence for the advancement of the proposed dynamic model and defect modeling method in this work.

5 Conclusions

This paper proposes a novel irregular shape defect modeling method and a dynamic model of double row cylindrical roller bearings, taking into account actual shapes of defects instead of simplified shapes. In this study, the effects of the bearing load, rotating speed, and different irregular defect shapes on vibrations were investigated. To validate the proposed model, a test was carried out, and the simulated vibrations and acceleration spectra of outer rings with rectangle defects, circular defects, and defects with irregular shapes were compared with experimental results. The results showed that the model results were in agreement with the experimental results, thus validating the defect modeling method and the proposed model. The key findings of the study are:

(1) The proposed irregular shape defect modeling method and dynamic model accurately simulate vibrations of double row cylindrical roller bearings with rectangular, circular, and irregular-shaped defects.
(2) Rotating speed has a significant impact on the acceleration RMS and PTP values of the inner/outer ring, rollers, and cage, with the inner ring having higher values than the outer ring, and the roller values increasing with increasing rotating speed.
(3) The TVCS of the actual defect is more accurate than that of the simplified defect, with differences observed in acceleration and impact when the roller enters and exits the defect. The model with the actual defect is more reasonable than that with the simplified defect.
(4) Rotating speed has a significant impact on the inner/outer ring and cage vibrations, with acceleration increasing and then decreasing with increasing rotating speed.

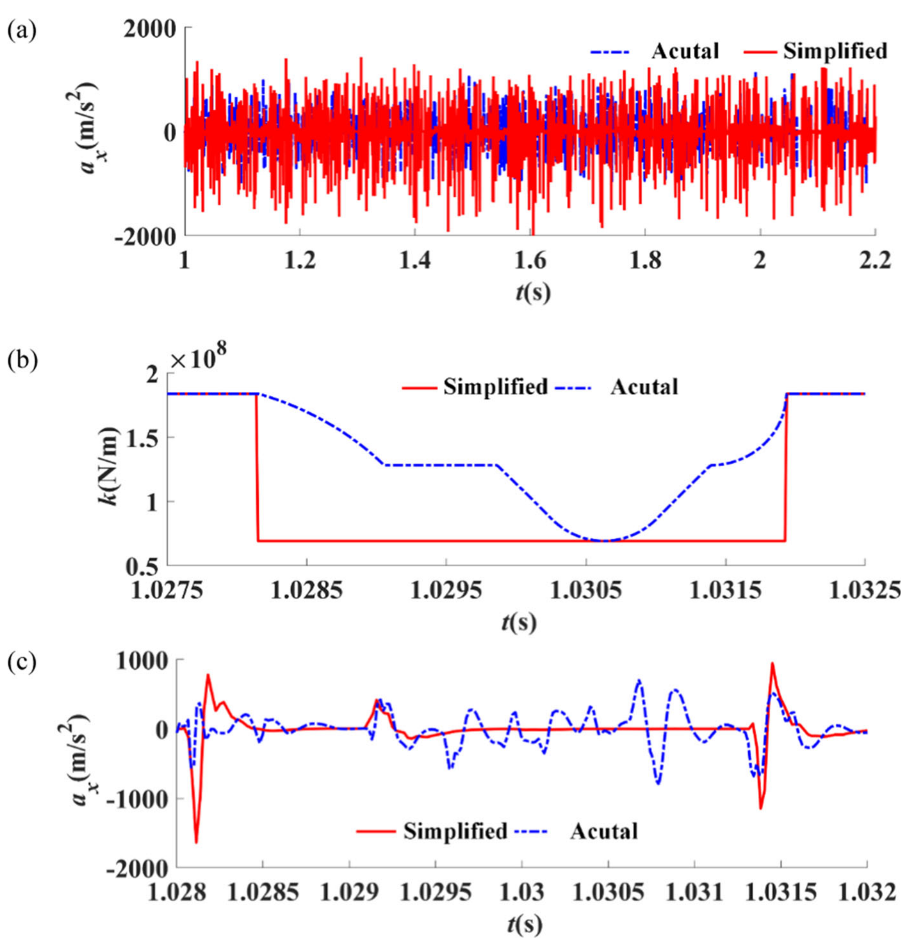

Fig. 14 Comparisons of **a** accelerations of outer ring, **b** TVCS, and **c** defect impact between the simplified defect shape and actual defect shape

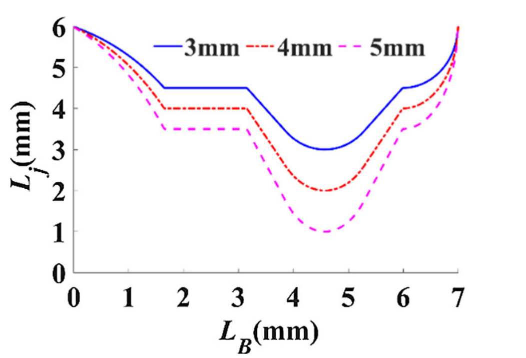

Fig. 15 Effective roller length when the roller rolls over the different defects

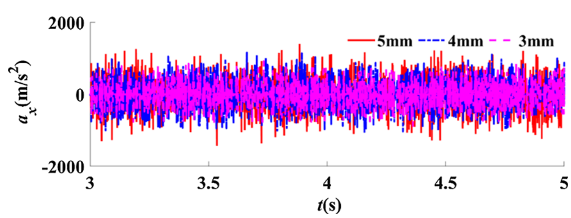

Fig. 16 Comparisons of accelerations of irregular defects with different maximum widths

(5) Load has a significant impact on the inner/outer ring and cage vibrations, with outer ring accelerations in the Y direction and inner ring accelerations increasing with increasing load value, and outer ring accelerations in the X direction and cage accelerations increasing and then decreasing with increasing load value.

(6) The simplified defect model will cause the bearing vibrations to be overestimated. The established dynamic model with the actual defect is more reasonable than the simplified defect model.

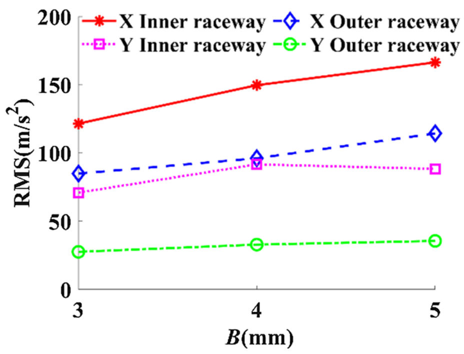

Fig. 17 Effect of the independent defect with different maximum widths on the accelerations of the inner/outer ring

Overall, the study provides valuable insights into the effects of rotating speed, load, and defect shape on double row cylindrical roller bearing vibrations and demonstrates the importance of considering actual defect shapes in dynamic models for engineering applications. However, there are also some aspects that need to be further studied. First, it is assumed that the defect morphology is ideal. However, the fault morphology is rough and uneven actually. The characteristics of the defect morphology have a significant impact on the contact stiffness between the roller and the ring. Besides, the defect edge elastic

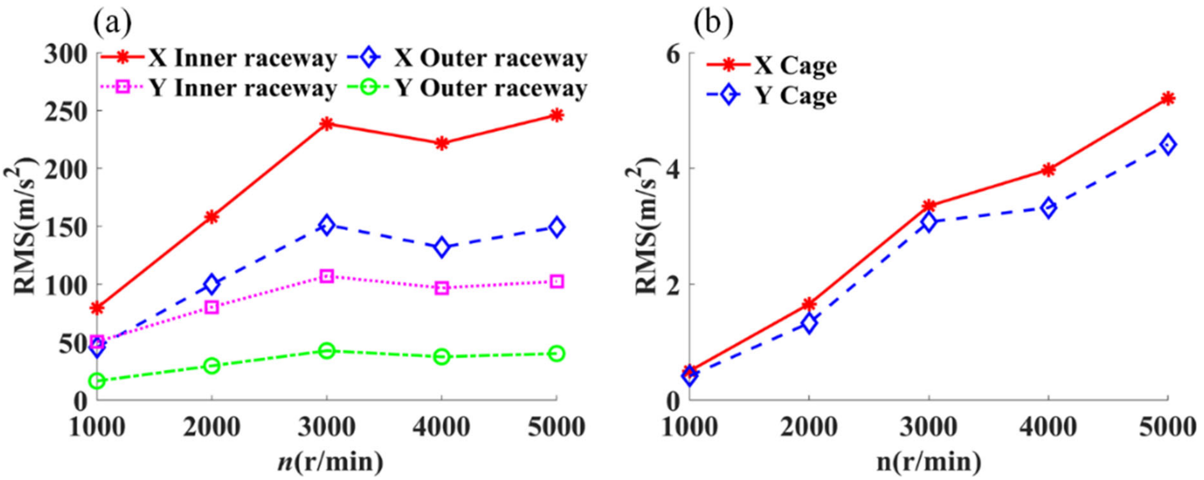

Fig. 18 Effect of the rotating speed on the inner/outer ring and cage accelerations. **a** RMS values of inner and outer ring accelerations and **b** RMS values of cage accelerations

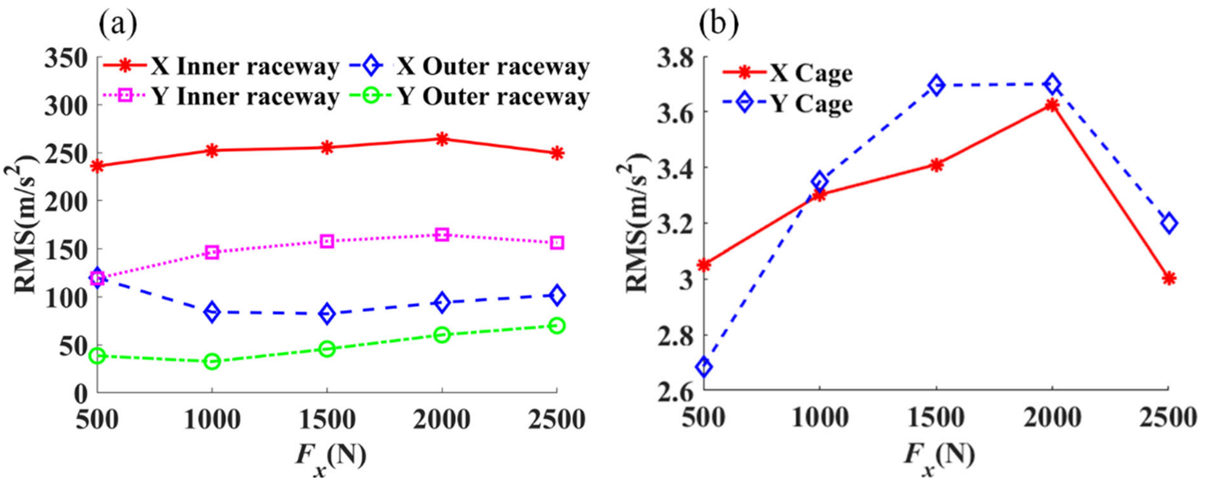

Fig. 19 Effect of the load value on the inner/outer ring and cage accelerations. **a** RMS values of inner and outer ring accelerations and **b** RMS values of cage accelerations

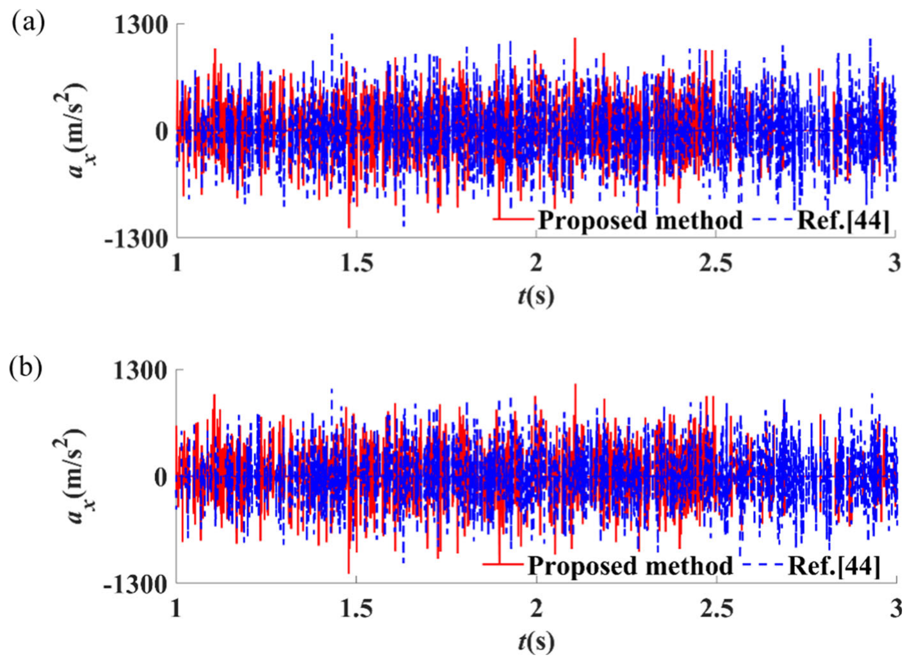

Fig. 20 Comparisons of accelerations obtained by **a**] the proposed dynamic model coupled with the proposed defect model and the proposed dynamic model in Ref. [43] coupled with the defect model in Ref. [43]; and **b** the proposed dynamic model coupled with the proposed defect model and the proposed dynamic model coupled with the defect model in Ref. [43]

deformation is ignored. Moreover, the double row cylindrical roller bearing is typically installed in rotor systems, and the effect of the irregular shape defect on the rotor system dynamics needs to be studied in future work.

Author contributions The author' contributions are as follows: XL wrote the manuscript, modelling and simulation analysis; JL was in charge of the whole trial; Shizhao Ding proposed modelling methods; YX proposed simulation analyses; YZ and MX revised the manuscript.

Funding Support provided by the National Natural Science Foundation of China under Contract No. 52211530085; Science Center for Gas Turbine Project (2022-B-III-003); Natural Science Foundation of Chongqing Contract No. CSTB2022NSCQ-MSX0318; and the Fundamental Research Funds for the Central Universities.

Data availability The datasets supporting the conclusions of this article are included within the article. The datasets are available from the corresponding author on reasonable request.

Declarations

Conflict of interest The authors have no conflicts of interest to this work.

Ethical approval Not applicable.

Consent for publication Not applicable.

References

1. Leblanc, A., Nelias, D., Defaye, C.: Nonlinear dynamic analysis of cylindrical roller bearing with flexible rings. J. Sound Vib. **325**(1–2), 145–160 (2009)
2. Li, X., Yu, K., Ma, H., et al.: Analysis of varying contact angles and load distributions in defective angular contact ball bearing. Eng. Fail. Anal. **91**, 449–464 (2018)
3. Arqub, O.A.: Numerical solutions for the Robin time-fractional partial differential equatioof heat and fluid flows based on the reproducing kernel algorithm. Int. J. Numer. Meth. Heat Fluid Flow **28**(4), 828–856 (2018)
4. Arqub, O.A., Shawagfeh, N.: Application of reproducing kernel algorithm for solving Dirichlet time-fractional diffusion-Gordon types equations in porous media. J. Porous Media **22**(4), 411–434 (2019)
5. Abu, A.O.: Numerical simulation of time-fractional partial differential equations arising in fluid flows via reproducing Kernel method. Int. J. Numer. Meth. Heat Fluid Flow **30**(11), 4711–4733 (2020)
6. Yang, Y., Yang, W., Jiang, D.: Simulation and experimental analysis of rolling element bearing fault in rotor-bearing-casing system. Eng. Fail. Anal. **92**, 205–221 (2018)
7. Xu, H., He, D., Ma, H., et al.: A method for calculating radial time-varying stiffness of flexible cylindrical roller bearings with localized defects. Eng. Fail. Anal. **128**, 105590 (2021)
8. Liu, X., Li, Y., Sun, M., et al.: A model of binaural auditory nerve oscillator network for bearing fault diagnosis by

integrating two-channel vibration signals. Nonlinear Dyn. **111**(5), 4779–4805 (2023)
9. Li, J., Zheng, J., Pan, H., et al.: Two-dimensional composite multi-scale time–frequency reverse dispersion entropy-based fault diagnosis for rolling bearing. Nonlinear Dyn. **111**(8), 7525–7546 (2023)
10. Liu, J., Shi, Z.F., Shao, Y.M.: An analytical model to predict vibrations of a cylindrical roller bearing with a localized surface defect. Nonlinear Dyn. **89**(3), 2085–2102 (2017)
11. Liu, J., Shao, Y.M.: An improved analytical model for a lubricated roller bearing including a localized defect with different edge shapes. J. Vib. Control **24**(17), 3894–3907 (2018)
12. Chen, A.Y., Kurfess, T.R.: A new model for rolling element bearing defect size estimation. Measurement **114**, 144–149 (2018)
13. Gao, P., Hou, L., Yang, R., et al.: Local defect modelling and nonlinear dynamic analysis for the inter-shaft bearing in a dual-rotor system. Appl. Math. Model. **68**, 29–47 (2019)
14. Cao, H.R., Su, S.M., Jing, X., et al.: Vibration mechanism analysis for cylindrical roller bearings with single/multi defects and compound faults. Mech. Syst. Signal Process. **144**, 106903 (2020)
15. Niu, L.K., Cao, H.R., Hou, H.P., et al.: Experimental observations and dynamic modeling of vibration, characteristics of a cylindrical roller bearing with roller defects. Mech. Syst. Signal Process. **138**, 106553 (2020)
16. Liu, J., Wang, L.: Dynamic modelling of combination imperfects of a cylindrical roller bearing. Eng. Fail. Anal. **135**, 106102 (2022)
17. Li, X., Liu, J., Shi, Z., et al.: Dynamic modeling of cylindrical roller bearings by considering non-through defects and additional forces. J. Multi Body Dyn. **237**(4), 666–680 (2023). https://doi.org/10.1177/14644193231189462
18. Arslan, H., Aktu, R.N.: An investigation of rolling element vibrations caused by local defects. J. Tribol. **130**(4), 1–12 (2008)
19. Patil, M.S., Mathew, J., Rajendrakumar, P.K., et al.: A theoretical model to predict the effect of localized defect on vibrations associated with ball bearing. Int. J. Mech. Sci. **52**(9), 1193–1201 (2010)
20. Patel, U.A., Naik, B.S.: Nonlinear vibration prediction of cylindrical roller bearing rotor system modeling for localized defect at inner race with finite element approach. J. Multi Body Dyn. **231**(4), 647–657 (2017)
21. Patel, U.K.A., Upadhyay, S.H.: Nonlinear dynamic response of cylindrical roller bearing-rotor system with 9 degree of freedom model having a combined localized defect at inner-outer races of bearing. Tribol. Trans. **60**(2), 284–299 (2017)
22. Safian, A., Zhang, H.S., Liang, X.H., et al.: Dynamic simulation of a cylindrical roller bearing with a local defect by combining finite element and lumped parameter models. Meas. Sci. Technol. **32**(12), 125111 (2021)
23. Jiang, Y.C., Huang, W.T., Luo, J.N., Wang, W.J.: An improved dynamic model of defective bearings considering the three-dimensional geometric relationship between the rolling element and defect area. Mech. Syst. Signal Process. **129**, 694–716 (2019)
24. Larizza, F., Howard, C.Q., Grainger, S.: Defect size estimation in rolling element bearings with angled leading and trailing edges. Struct. Health Monit. **20**(3), 1102–1116 (2021)
25. Wang, X., Mao, D., Li, X.: Bearing fault diagnosis based on vibro-acoustic data fusion and 1D-CNN network. Measurement **173**, 108518 (2021)
26. Liu, J., Wang, L., Shi, Z.: Dynamic modelling of the defect extension and appearance in a cylindrical roller bearing. Mech. Syst. Signal Process. **173**, 109040 (2022)
27. Liu, J., Xu, Z., Xu, Y., et al.: An analytical method for dynamic analysis of a ball bearing with offset and bias local defects in the outer race. J. Sound Vib. **461**, 114919 (2019)
28. Gao, S., Chatterton, S., Pennacchi, P., et al.: Behaviour of an angular contact ball bearing with three-dimensional cubic-like defect: a comprehensive non-linear dynamic model for predicting vibration response. Mech. Mach. Theory **163**, 104376 (2021)
29. De Angelis, F., Taylor, R.L.: A nonlinear finite element plasticity formulation without matrix inversions. Finite Elem. Anal. Des. **112**, 11–25 (2016)
30. De Angelis, F., Taylor, R.L.: An efficient return mapping algorithm for elastoplasticity with exact closed form solution of the local constitutive problem. Eng. Comput. **32**(8), 2259–2291 (2015)
31. Liu, J., Shao, Y.: Dynamic modeling for rigid rotor bearing systems with a localized defect considering additional deformations at the sharp edges. J. Sound Vib. **398**, 84–102 (2017)
32. De Angelis, F.: Computational issues and numerical applications in rate-dependent plasticity. Adv. Sci. Lett. **19**(8), 2359–2362 (2013)
33. Luo, Y., Baddour, N., Liang, M.: A shape-independent approach to modelling gear tooth spalls for time varying mesh stiffness evaluation of a spur gear pair. Mech. Syst. Signal Process. **120**(1), 836–852 (2019)
34. Tu, W., Yu, W., Shao, Y., et al.: A nonlinear dynamic vibration model of cylindrical roller bearing considering skidding. Nonlinear Dyn. **103**, 2299–2313 (2021)
35. Harris, T.A.: Essential concepts of bearing technology. In: Rolling Bearing Analysis, p. 200 (2006)
36. De Angelis, F., Cancellara, D.: Multifield variational principles and computational aspects in rate plasticity. Comput. Struct. **180**, 27–39 (2017)
37. Tu, W., Liang, J., Yu, W., et al.: Motion stability analysis of cage of rolling bearing under the variable-speed condition. Nonlinear Dyn. **111**, 1–19 (2023)
38. Shi, Z., Liu, J.: An improved planar dynamic model for vibration analysis of a cylindrical roller bearing. Mech. Mach. Theory **153**, 103994 (2020)
39. Liu, J., Ni, H., Zhou, R., Li, X., Xing, Q., Pan, G.: A simulation analysis of ball bearing lubrication characteristics considering the cage clearance. J. Tribol. **145**(4), 044301 (2023)

40. Li, X., Liu, J., Xu, J., et al.: A vibration model of a planetary bearing system considering the time-varying wear. Nonlinear Dyn. **111**, 1–24 (2023)
41. Liu, J., Li, X., Xia, M.: A dynamic model for the planetary bearings in a double planetary gear set. Mech. Syst. Signal Process. **194**, 110257 (2023)
42. Liu, J., Li, X., Pang, R., et al.: Dynamic modeling and vibration analysis of a flexible gear transmission system. Mech. Syst. Signal Process. **197**, 110367 (2023)
43. Lin, S., Sun, J., Ma, C., et al.: A novel dynamic modeling method of defective four-row roller bearings considering the spatial contact correlation between the roller and defect zone. Mech. Mach. Theory **180**, 105138 (2023)